

Energy Dependent Features of X-ray Signals in a GridPix Detector

C. Krieger^a, J. Kaminski^{a,*}, T. Vafeiadis^b, K. Desch^a

^a*Physikalisches Institut, University of Bonn, Germany*

^b*CERN, Geneva, Switzerland*

Abstract

We report on the calibration of an argon/isobutane (97.7%/2.3%)-filled GridPix detector with soft X-rays (277 eV to 8 keV) using the variable energy X-ray source of the CAST Detector Lab at CERN. We study the linearity and energy resolution of the detector using both the number of hit pixels and the total measured charge as energy measures. For the latter, the energy resolution σ_E/E is better than 10% (20%) for energies above 2 keV (0.5 keV). Several characteristics of the recorded events are studied.

Keywords: Timepix, InGrid, GridPix, X-ray, CAST

1. Introduction and Description of Setup

Gaseous X-ray detectors with a high granularity readout have advantages over other detector types, such as silicon detectors, if additional information based on the event shape is required to suppress non-X-ray background. One application is the search for axions and chameleons, where a main background stems from cosmic rays passing through the detector. The CAST experiment at CERN uses the helioscope technique by pointing a strong magnet towards the Sun and searching with various detectors for new particles, which convert into X-ray photons inside the magnetic field. CAST is currently setting stringent limits on both axion [1] and Solar chameleon searches [2]. To further improve the sensitivity, we have shown that exploiting topological features of a signal is a very powerful technique and can be performed with a GridPix detector [3]. We have, therefore, studied the features of X-ray events of various energies with the help of an X-ray gun setup at the CAST Detector Lab at CERN [4].

1.1. X-ray Generation

The CAST Detector Lab provides a dedicated setup where X-ray photons of various energies can be generated. For this, an electron beam is directed on

*Corresponding author

Email address: kaminski@physik.uni-bonn.de (J. Kaminski)

setup	beam energy	target material	filter	fluorescence line(s)
A	15 keV	copper	nickel	Cu K_{α} (8.048 keV)
B	12 keV	manganese	chromium	Mn K_{α} (5.899 keV)
C	9 keV	titanium	titanium	Ti K_{α} (4.511 keV) Ti K_{β} (4.932 keV)
D	6 keV	silver	silver	Ag L_{α} (2.984 keV) Ag L_{β} (3.151 keV)
E	4 keV	aluminum	aluminum	Al K_{α} (1.487 keV)
F	2 keV	copper	EPIC	Cu L_{α} (0.930 keV) Cu L_{β} (0.950 keV)
G	0.9 keV	copper	EPIC	O K_{α} (0.525 keV)
H	0.6 keV	carbon	EPIC	C K_{α} (0.277 keV)

Table 1: Beam energies, target and filter materials chosen to produce photons of the listed fluorescence lines by an X-ray generator. A letter is assigned to each setup for reference throughout this document. For some settings more than one fluorescence line is listed, in these cases there was no adequate filter material available to suppress the unwanted line, e.g. the K_{β} lines of several target elements. The filter material EPIC is a composite filter composed of a 330 nm thick polypropylene carrier sandwiched by two 90 nm aluminum layers with a 35 nm tin layer on top of one side, also known as *Thick filter* and developed as UV filter for the European Photon Imaging Cameras utilized in the XMM-Newton satellite [5]. The energies of the lines were taken from the X-ray data booklet [6].

a target creating an X-ray spectrum containing the well known characteristic X-ray fluorescence lines of the target material on top of a broad Bremsstrahlung continuum. A dedicated filter is then used to isolate the selected characteristic lines or suppress unwanted parts of the spectrum as good as possible. By adjusting the electron beam energy, the target material and the filter material, quite clean spectra can be created. The settings used are given in Table 1. The photons are then guided through a vacuum pipe to the detector. The maximum rate of X-ray photons entering the detector is limited by the filters and windows that were used and by the maximum beam current tolerable for the passive cooled target. This limitation in the X-ray photon rate only affects energies below 2 keV while the detector’s readout time of 25 ms affects all energies as the readout rate is limited to 40 Hz resulting in a fairly low duty cycle depending on the chosen acquisition times. Therefore, collecting about 10 000 photons took more than one hour for each energy setting.

1.2. Detector

The detector is described in detail in reference [7]. A short summary of the important features is given here. The readout is based on a GridPix, which consists of a Timepix ASIC [8] on top of which a Micromegas gas amplification stage (InGrid) is built by photolithographic post-processing techniques [9, 10]. The good alignment of each mesh hole with one readout pixel of the ASIC and low charge threshold of the pixel are features of the setup: If a primary electron

enters in one mesh hole, the electron avalanche of the gas amplification is collected by a single readout pixel with a typical threshold of about 700 electrons. Thus, each primary electron can be detected with a very high efficiency [11], if primary electrons do not end up on the grid and diffusion spreads the charge cloud sufficiently, so that multiple electrons do not enter the same mesh hole.

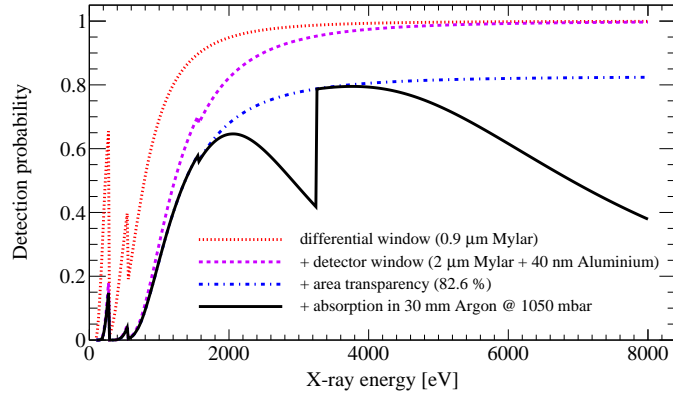
The drift volume has a maximum drift distance of 3 cm and is filled with an argon based mixture containing 2.3% isobutane as quencher. A drift field of 500 V/cm is applied. The cathode is made of a solid 3 mm copper plate, where 5×5 windows of $3 \times 3 \text{ mm}^2$ each have been cut out. The optical transparency of this strong-back is 82.6%. A 2 μm thick Mylar foil with a 40 nm layer of aluminum was glued on the copper to achieve gas tightness between the drift volume and the vacuum of the X-ray generator. A differential pumping is, however, still necessary and requires an additional window consisting of a 0.9 μm thick Mylar foil separating the good vacuum of the X-ray generator ($p \approx 2 \times 10^{-6}$ mbar) from the bad vacuum ($p < 5 \times 10^{-4}$ mbar) close to the detector. The transmission probability through the two windows and the detection efficiency as a function of the X-ray energy are shown in Fig. 1.

1.3. Analysis

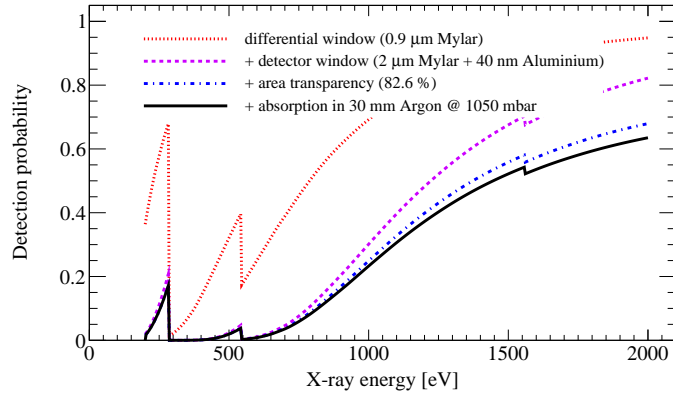
X-ray events are recorded through an unbiased frame-based acquisition. A logical shutter opens for 600 μs and then the whole Timepix ASIC is readout. For each hit pixel, the time-over-threshold (ToT) is recorded in a 14-bit pseudo-random counter and used as measure of the collected charge by applying a charge calibration. From the recorded event samples, clean X-ray events are selected employing a number of offline selection cuts. A first cut requires at least three activated pixels in the event to reject empty frames. The remaining events are then analyzed using the MarlinTPC software framework [13]. Here the X-ray photons are reconstructed by searching for a first seed pixel starting at the top left corner. Additional electrons are assigned to the X-ray by searching in a 50 by 50 pixels array (each pixel measures $55 \times 55 \mu\text{m}^2$), around each pixel already found. For every pixel assigned to the X-ray the same search will be performed in its vicinity. In this way all pixels belonging to one X-ray photon are identified and X-ray photons far apart from each other are reconstructed separately. Fig. 2 shows the charge clouds of two X-ray photons: one with an energy of 277 eV and one with 8 keV.

Several properties of each charge cloud are determined. The position of the X-ray conversion is determined by calculating the mean of all pixel positions in x and y direction. The mean is required to be less than 4.5 mm from the center of the active area. This ensures a minimal distance of 2.5 mm to the edges, so that even with maximal charge cloud size of $\sigma(3 \text{ cm}) = D_T \cdot \sqrt{z} = 470 \mu\text{m}/\sqrt{\text{cm}} \cdot \sqrt{3 \text{ cm}} \approx 815 \mu\text{m}$ almost no electrons are lost outside of the sensitive area. Here D_T is the transverse diffusion coefficient for the argon based gas mixture used.

The energy was determined by two different methods: In the first approach the number of activated pixels gives a very good estimate of the number of primary electrons, which multiplied by the average ionization energy W_I yields the energy of the X-ray photon. In the second approach, the total charge Q can



(a)



(b)

Figure 1: The graph in (a) shows the transmission probability as a function of the X-ray energy through the differential window, the transmission through the differential and detector window, transmission through the differential and detector window including the area transparency of the window strong back and the final detection probability including the previous transmissions and the absorption in argon. (b) shows a detailed view of the low energy range. Transmission and absorption data have been produced by a generator using the semi-empirical approach described in [12]. Graphs and caption taken from [7].

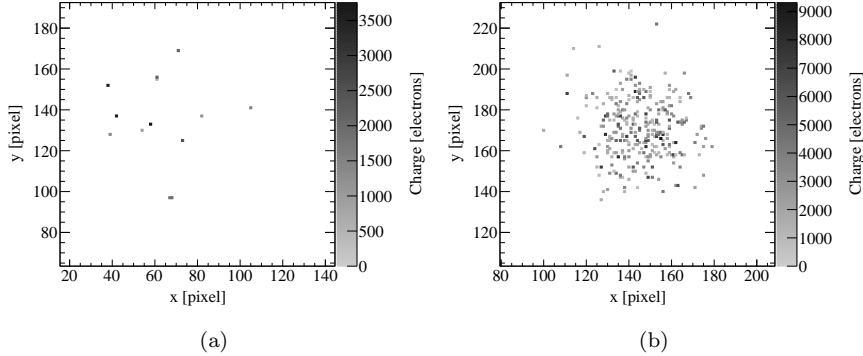


Figure 2: The two images show clusters of a 277 eV X-ray photon (a) and of an 8 keV X-ray photon (b). Both pictures show only an enlargement of the event and not the full sensitive area.

be determined by summing over the charge collected by all pixels assigned to the X-ray photon. The total charge Q is then used as a measure of the energy of the X-ray photon times the gas gain G and divided by the ionization energy W_I .

The spatial width of the charge clouds is slightly asymmetric. This is mostly because of statistical fluctuations in the diffusion process and can be measured by the eccentricity of the event. For higher X-ray energies, also the length of the track of the photoelectron ejected from the atom with an energy exceeding the binding energy contributes to the asymmetry (e.g. a 5 keV electron has a range of about $500 \mu\text{m}$ in argon/isobutane 97.7%/2.3% at 1050 mbar). We have, therefore, identified the longest axis of the charge cloud and perpendicular to this the shortest axis. The rms of the charge cloud in the direction of the shorter (= transverse) axis is referred to as σ_{trans} and indicates the diffusion, while the rms value of the pixel position projected on the long event axis gives σ_{long} .

Finally, topological parameters such as longest axis and event shape variables such as eccentricity and higher central moments (e.g. kurtosis) are calculated within this event specific coordinate system. These parameters are correlated with the diffusion and are therefore temperature dependent. To avoid this dependence the following three parameters were defined as ratios. These parameters can be used as variables to distinguish X-ray events from charged particle background, e.g. in the analysis of CAST data.

1. Fraction $F_{1\sigma_{\text{trans}}}$ of pixels within radius of $1 \sigma_{\text{trans}}$ around center
2. Eccentricity $\epsilon = \sigma_{\text{long}}/\sigma_{\text{trans}}$: a measure for the circularity of an event. By construction, ϵ is always larger or equal to 1.
3. Length l divided by σ_{trans} : The length is defined as the distance of the outermost points in the projection onto the long event axis.

setup	applied cuts
A	$\epsilon < 1.3, 0.1 \text{ mm} < \sigma_{\text{trans}} \leq 1.0 \text{ mm}$
B	$\epsilon < 1.3, 0.1 \text{ mm} < \sigma_{\text{trans}} \leq 1.0 \text{ mm}$
C	$\epsilon < 1.3, 0.1 \text{ mm} < \sigma_{\text{trans}} \leq 1.0 \text{ mm}$
D	$\epsilon < 1.4, 0.1 \text{ mm} < \sigma_{\text{trans}} \leq 1.0 \text{ mm}, l \leq 6 \text{ mm}$
E	$\epsilon < 2.0, 0.1 \text{ mm} < \sigma_{\text{trans}} \leq 1.1 \text{ mm}$
F	$\epsilon < 2.0, 0.1 \text{ mm} < \sigma_{\text{trans}} \leq 1.1 \text{ mm}$
G	$\epsilon < 2.0, 0.1 \text{ mm} < \sigma_{\text{trans}} \leq 1.1 \text{ mm}$
H	$0.1 \text{ mm} < \sigma_{\text{trans}} \leq 1.1 \text{ mm}, l \leq 6 \text{ mm}$

Table 2: Cuts on eccentricity ϵ , transverse rms σ_{trans} and length l , applied to the data recorded with the different X-ray gun setups. Cut values are chosen rather loose in order to only reject events incompatible with the single photon hypothesis. Additionally, for all setups a minimum number of 3 active pixels is required to reject empty events. Also, all accepted events are required to have their center of gravity within a 4.5 mm radius around the chip center to avoid events only partially contained in the active area.

Due to insufficient matching of the shutter times to the photon rate provided by the X-ray generator some of the datasets contain a significant fraction of double events where the two or more X-ray photons cannot be separated by the algorithm. To filter out these events, loose cuts on eccentricity ϵ , length l , and transverse rms σ_{trans} were applied, the cuts for each setup are listed in Table 2. In case of l and σ_{trans} the cuts were chosen such that only events incompatible with the single photon hypothesis were rejected.

2. Spectra and Energy Calibration

For each electron beam energy, target and filter combination described in Table 1, the resulting spectrum was created. They are shown in Figs. 3 and 4, using the number of primary electrons (left column) and the total charge (right column) as measure for the detected energy.

Some of the spectra, in addition to the main peak, contain extra peaks due to different processes or causes. For energies above 3 keV the argon escape line of the main line appears; e.g. in the spectrum of setup C (see Figs. 3e and 3f) the argon escape line is visible approximately 3 keV below the main titanium K_{α} line at 4.5 keV. Especially for the low energies, additional fluorescence lines show up, close to the main line which can be attributed to contaminations of the target material. For example the prominent carbon line (see Figs. 4g and 4h) also has a visible shoulder at higher energies corresponding to the oxygen K_{α} line at 525 eV which is produced by a small oxygen contamination of the target surface. All lines considered in the fits are listed in table 3.

The main peak is always described by a Gaussian function with three free parameters: amplitude of the Gaussian N , position of mean μ and width σ . Some parameters of the side peaks are linked to values of the main peak. For example, the same width is used, if the side peak is sufficiently close, or the

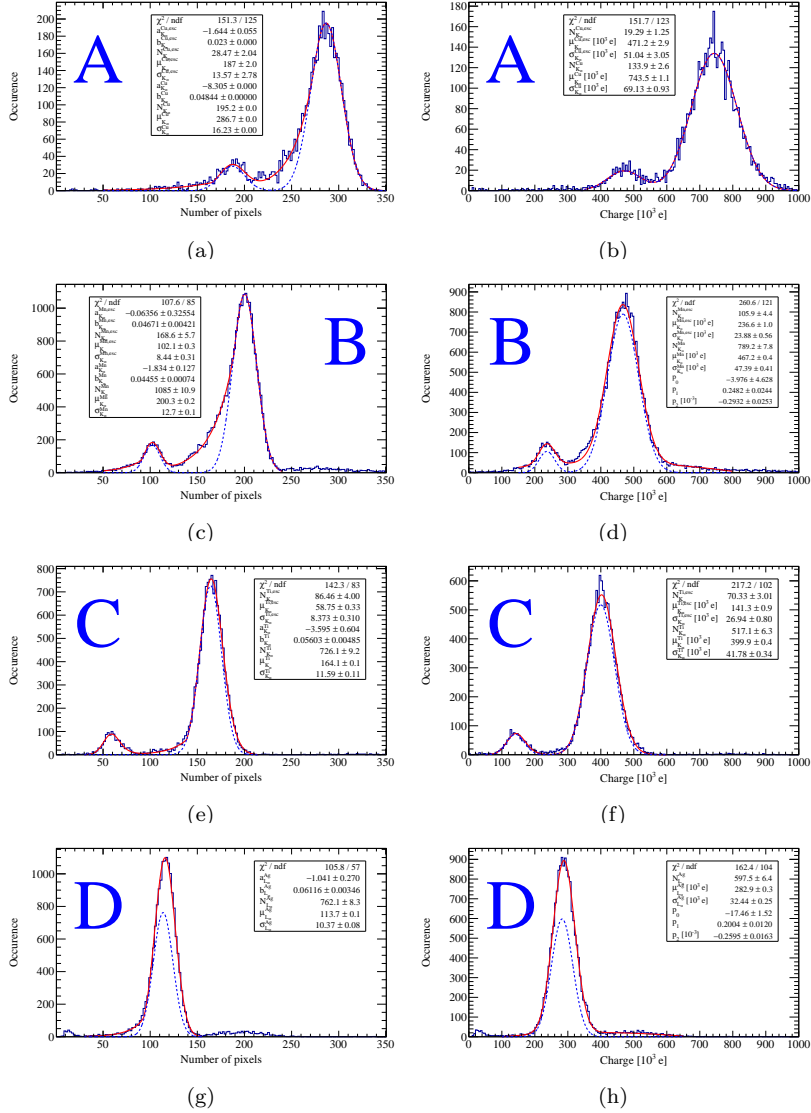


Figure 3: Energy spectra of various settings based on the number of primary electrons (left) and total charge (right). Main peaks shown are the copper K_{α} line at 8 keV: (a) and (b); the manganese K_{α} line at 5.9 keV: (c) and (d); the titanium K_{α} line at 4.5 keV: (e) and (f); and the silver L_{α} line at 3 keV: (g) and (h). The functions fitted to the spectra are shown in solid red while the Gaussians describing the main peaks are plotted in addition as blue dashed line.

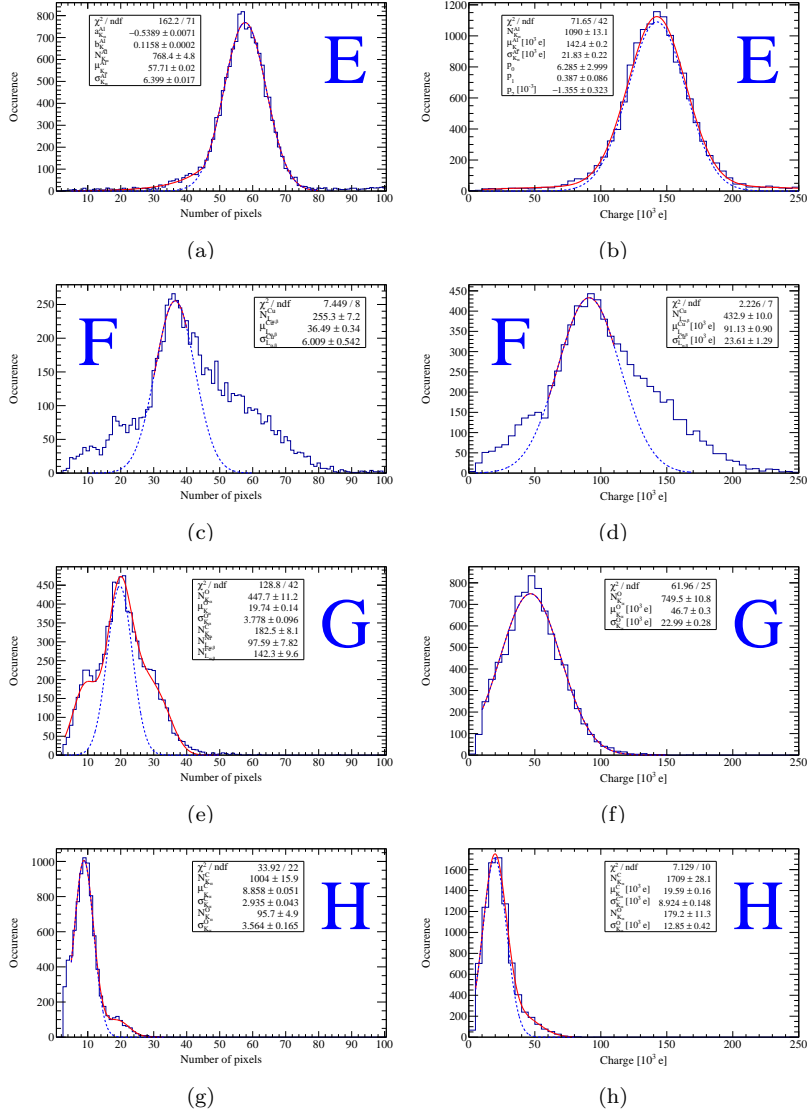


Figure 4: Energy spectra of various settings based on the number of primary electrons (left) and total charge (right). Main peaks shown are the aluminum K_α line at 1.5 keV: (a) and (b); the copper L_α line at 0.9 keV: (c) and (d); the oxygen K_α line at 0.5 keV: (e) and (f); and the carbon K_α line at 277 eV: g and (h). The functions fitted to the spectra are shown in solid red while the Gaussians describing the main peaks are plotted in addition as blue dashed line.

fluorescence line	additional peaks	fixed parameters
Cu K_α (8.048 keV)	Cu K_α escape (5.057 keV)	none
Mn K_α (5.899 keV)	Mn K_α escape (2.925 keV)	none
Ti K_α (4.511 keV)	Ti K_β (4.932 keV) Ti K_α escape (1.537 keV) Ti K_β escape(1.959 keV)	$\mu_{K_\beta}^{\text{Ti}}, \sigma_{K_\beta}^{\text{Ti}}, N_{K_\beta}^{\text{Ti}}/N_{K_\alpha}^{\text{Ti}}$ $\mu_{K_\beta}^{\text{Ti-esc}}, \sigma_{K_\beta}^{\text{Ti-esc}}$
Ag L_α (2.984 keV)	Ag L_β (3.151 keV)	$\mu_{L_\beta}^{\text{Ag}}, \sigma_{L_\beta}^{\text{Ag}}, N_{L_\beta}^{\text{Ag}}/N_{L_\alpha}^{\text{Ag}}$
Al K_α (1.487 keV)	none	none
Cu L_α (0.930 keV)	see note in caption	see note in caption
O K_α (0.525 keV)	C K_α (0.277 keV) Fe $L_{\alpha,\beta}$ (0.71 keV) Ni $L_{\alpha,\beta}$ (0.86 keV)	$\mu_{K_\alpha}^{\text{C}}, \sigma_{K_\alpha}^{\text{C}}$ $\mu_{K_{\alpha,\beta}}^{\text{Fe}}, \sigma_{K_{\alpha,\beta}}^{\text{Fe}}$ $\mu_{K_{\alpha,\beta}}^{\text{Ni}}, \sigma_{K_{\alpha,\beta}}^{\text{Ni}}$
C K_α (0.277 keV)	O K_α (0.525 keV)	$\mu_{K_\alpha}^{\text{O}}, \sigma_{K_\alpha}^{\text{O}}$

Table 3: X-ray lines visible in the different spectra. For some of the spectra additional lines have to be taken into account in the fitted functions which stem from argon escape lines, close-by β lines and/or additional elements present in the target material (possible contaminations). To simplify the fits as many parameters as possible have been fixed for the additional lines: The mean μ of the fitted Gaussian is usually fixed relative to the position of the main peak while the width σ is assumed to be the same as for the close-by main peak. For β lines also the relative intensity is used to fully fix the additional peak through the main peak. In case of the copper L_α line there are definitely contributions by other X-ray lines visible in the spectrum but no neighboring peaks could be clearly identified, therefore in this case the fit range was narrowed to the main peak. In case of the oxygen K_α line many contaminants show up, possibly present in the form of stainless steel screws used to mount the target. Additional peaks were identified using the tabulated X-ray fluorescence energies in [6] from which also the information used to fix some of the fit parameters were taken.

setup	fit function
A	$EG_{K_\alpha}^{\text{Cu,esc}}(a, b, N, \mu, \sigma) + EG_{K_\alpha}^{\text{Cu}}(a, b, N, \mu, \sigma)$
B	$EG_{K_\alpha}^{\text{Mn,esc}}(a, b, N, \mu, \sigma) + EG_{K_\alpha}^{\text{Mn}}(a, b, N, \mu, \sigma)$
C	$G_{K_\alpha}^{\text{Ti,esc}}(N, \mu, \sigma) + G_{K_\beta}^{\text{Ti,esc}}(N, \mu, \sigma)$ $+ EG_{K_\alpha}^{\text{Ti}}(a, b, N, \mu, \sigma) + G_{K_\beta}^{\text{Ti}}(N, \mu, \sigma)$
D	$EG_{L_\alpha}^{\text{Ag}}(a, b, N, \mu, \sigma) + G_{L_\beta}^{\text{Ag}}(N, \mu, \sigma)$
E	$EG_{K_\alpha}^{\text{Al}}(a, b, N, \mu, \sigma)$
F	$G_{L_{\alpha,\beta}}^{\text{Cu}}(N, \mu, \sigma)$
G	$G_{K_\alpha}^{\text{O}}(N, \mu, \sigma) + G_{K_\alpha}^{\text{C}}(N, \mu, \sigma)$ $+ G_{L_{\alpha,\beta}}^{\text{Fe}}(N, \mu, \sigma) + G_{L_{\alpha,\beta}}^{\text{Ni}}(N, \mu, \sigma)$
H	$G_{K_\alpha}^{\text{C}}(N, \mu, \sigma) + G_{K_\alpha}^{\text{O}}(N, \mu, \sigma)$

Table 4: Fit functions used for the pixel spectra in Figs. 3 and 4. A Gaussian with amplitude N , mean μ and width σ is abbreviated with $G(N, \mu, \sigma)$ while the Gaussian joined with an exponential decay to the left (see Equation 1) is noted as $EG(a, b, N, \mu, \sigma)$. The upper and lower indices of the parameters are noted at the function itself as all parameters of a function share the same indices, e.g. $G(N_\alpha, \mu_\alpha, \sigma_\alpha)$ will be noted as $G_\alpha(N, \mu, \sigma)$. Not all parameters were left free for the fits, Table 3 lists the parameters fixed for each setting.

position is fixed, if the relative or fractional energy difference is known. The list of the fixed parameters is also given in Table 3, the full fit functions used are listed in Tables 4 and 5. For some of the spectra polynomial terms are added to the fit to describe the background in the spectra most probably caused by remnant double events.

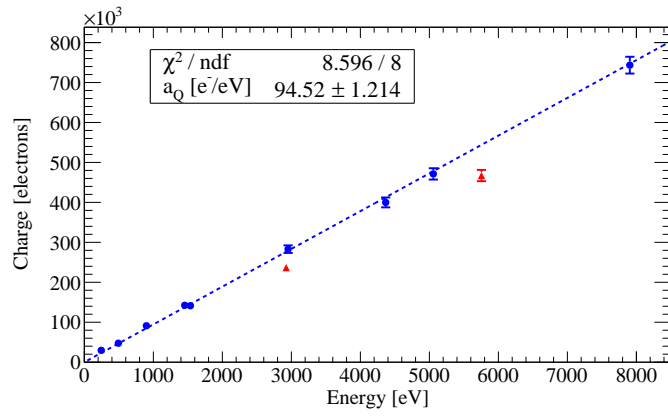
In case of the pixel spectra, the lines of higher X-ray energies show a tail towards lower energies. This can be explained by insufficient diffusion, which leads to two electrons being guided into the same grid hole and detected as a single primary electron. This is the case mostly for more energetic X-rays having a higher charge density in the center of the charge cloud and a longer absorption length, resulting in less diffusion. To take this into account, the Gaussian function was joined by an exponential function:

$$f(x) = \begin{cases} N \exp^{-\frac{(x-\mu)^2}{2\sigma^2}} & \text{for } : x > c \\ \exp^{ax+b} & \text{for } : x < c \end{cases} \quad (1)$$

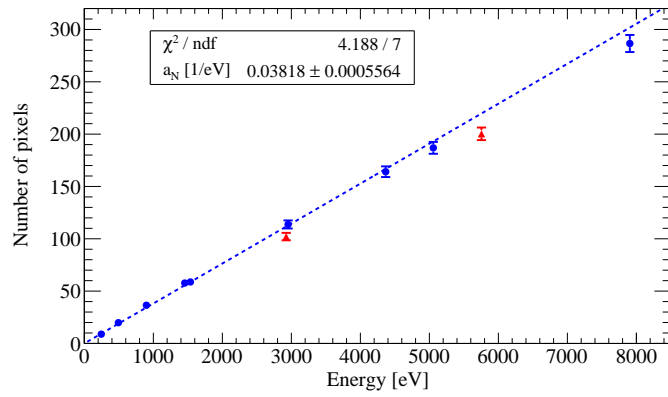
a and b parameterize the exponential decay. The parameter c , defining the junction point of the two functions, is determined by the parameters of the two functions to allow for a continuous function.

The fitted peak positions of different X-ray photon energies are shown in Fig. 5 resulting in a calibration curve for both the total charge and the number of activated pixels.

The y -intercept was set to zero and only the slope a was determined by the fit giving the conversion factor form either charge (a_Q) or number of pixels (a_N) to X-ray photon energy. In both graphs the measurement with the manganese



(a)



(b)

Figure 5: Graphs showing the total charge (a) and number of activated pixels (b) in dependence on the X-ray photon energy. The manganese lines are not used for the fits and marked as red triangles. The point corresponding to the 8 keV copper line in (b) was excluded from the fit.

setup	fit function
A	$G_{K_\alpha}^{\text{Cu,esc}}(N, \mu, \sigma) + G_{K_\alpha}^{\text{Cu}}(N, \mu, \sigma)$
B	$G_{K_\alpha}^{\text{Mn,esc}}(N, \mu, \sigma) + G_{K_\alpha}^{\text{Mn}}(N, \mu, \sigma) + p_0 + p_1 \cdot x + p_2 \cdot x^2$
C	$G_{K_\alpha}^{\text{Ti,esc}}(N, \mu, \sigma) + G_{K_\beta}^{\text{Ti,esc}}(N, \mu, \sigma)$ $+ G_{K_\alpha}^{\text{Ti}}(N, \mu, \sigma) + G_{K_\beta}^{\text{Ti}}(N, \mu, \sigma)$
D	$G_{L_\alpha}^{\text{Ag}}(N, \mu, \sigma) + G_{L_\beta}^{\text{Ag}}(N, \mu, \sigma) + p_0 + p_1 \cdot x + p_2 \cdot x^2$
E	$G_{K_\alpha}^{\text{Al}}(N, \mu, \sigma) + p_0 + p_1 \cdot x + p_2 \cdot x^2$
F	$G_{L_{\alpha,\beta}}^{\text{Cu}}(N, \mu, \sigma)$
G	$G_{K_\alpha}^{\text{O}}(N, \mu, \sigma)$
H	$G_{K_\alpha}^{\text{C}}(N, \mu, \sigma) + G_{K_\alpha}^{\text{O}}(N, \mu, \sigma)$

Table 5: Fit functions used for the charge spectra on Figs. 3 and 4. A Gaussian with amplitude N , mean μ and width σ is abbreviated with $G(N, \mu, \sigma)$. The upper and lower indices of the parameters are noted at the function itself as all parameters of a function share the same indices, e.g. $G(N_\alpha, \mu_\alpha, \sigma_\alpha)$ will be noted as $G_\alpha(N, \mu, \sigma)$. Not all parameters were left free for the fits, Table 3 lists the parameters fixed for each setting.

K_α line at 5.9 keV is deviating from the fit curve. It was found that the temperature in the laboratory, and consequently in the detector as well, was lower by approximately 5 to 10 °C during this measurement and therefore the gas gain was reduced. It can also be observed, that for high energies (e.g. 8 keV) the number of pixels is below the calibration curve, because for large enough numbers of primary electrons the diffusion is always insufficient to prevent multiple electrons entering the same grid hole in the center of the photon clusters. To avoid any bias in the calibration curve, all manganese lines as well as the 8 keV in the pixel spectrum were not considered in the fit.

Since the slopes of the calibration curves give the number of pixels per eV and the measured charge per eV respectively, the gas gain can be determined by $G_a = a_Q/a_N \approx 2500$ from a_Q and a_N . The inverse of a_N should also give the mean ionization energy W_I and indeed $a_N^{-1} \approx 26$ eV which matches the tabulated values for argon and isobutane.

The energy resolution can be defined as $\sigma_E/E = \sigma/\mu$, where σ is the width and μ the position of the line under consideration. The values have been extracted from the fits and are shown for both energy measurement methods in Fig. 6.

The energy resolution improves with $\sqrt{a^2/E + b^2}$ where a/\sqrt{E} describes the statistical part of the energy resolution. As expected the resolution improves with the number of primary electrons ($E \propto N$). b denotes the systematical contribution to the total energy resolution which is added quadratically.

Finally, the gas amplification can also be extracted independently of the calibration curve by histogramming the charge collected by each pixel. Fig. 7 shows three different distributions: one filled with pixels' charges from 1.5 keV X-ray events, two filled with charges collected on individual pixels from 8 keV X-ray events but only using those primary electrons (pixels) which are at least

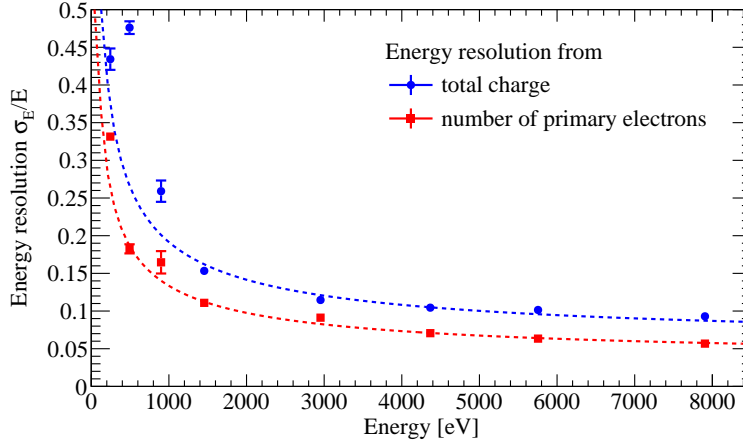


Figure 6: Energy resolution σ_E/E in dependence of the X-ray photon energy. As the energy can be determined from either the number of activated pixels (detected primary electrons) or the total charge of a reconstructed X-ray photon, the energy resolution for both methods is shown. In both cases the energy dependence is well described by $1/\sqrt{E}$. The deviation of a few points at low energies is caused by those spectra containing additional peaks (e.g. from target contaminations) which cannot be separated from the main peak thus leading to an overestimation of the peak width.

1.75 mm from the event center and those with a maximum distance of 1 mm to the event center respectively. The distributions are fitted to a Polya-function. The parameterization is given by [14]:

$$P_{\text{Polya}}(x) = \frac{K}{G_{\text{Polya}}} \frac{(\Theta + 1)^{\Theta+1}}{\Gamma(\Theta + 1)} \left(\frac{x}{G_{\text{Polya}}} \right)^{\Theta} \exp \left(-(\Theta + 1) \frac{x}{G_{\text{Polya}}} \right) \quad (2)$$

where K is a scaling parameter to adopt the normalized distribution to the data, G_{Polya} is a measure for the gas gain (but cannot be directly compared to the mean or MPV of the distribution) and Θ is inverse proportional to the width of the distribution. As expected the first two distributions are in good agreement and show a Polya distribution. From the fit the gas gain can be extracted to be $G_{\text{Polya}} \approx 3000$. Taking the mean of the distributions one gets $G_{\text{mean}} \approx 2500$ ($G_{\text{MPV}} \approx 2200$) which is in good agreement with G_a . However, the distribution given by pixels in the center of the 8 keV X-ray photon charge clouds becomes notably broader. This can be explained by contributions of pixels with two electrons collected. This also leads to an overestimation of the mean gas gain.

3. Additional Features of the Events

Fig. 8 shows the histogram of the cluster widths σ_{trans} for two different X-ray energies. Both distributions reach a maximum slightly above 0.8 mm which is

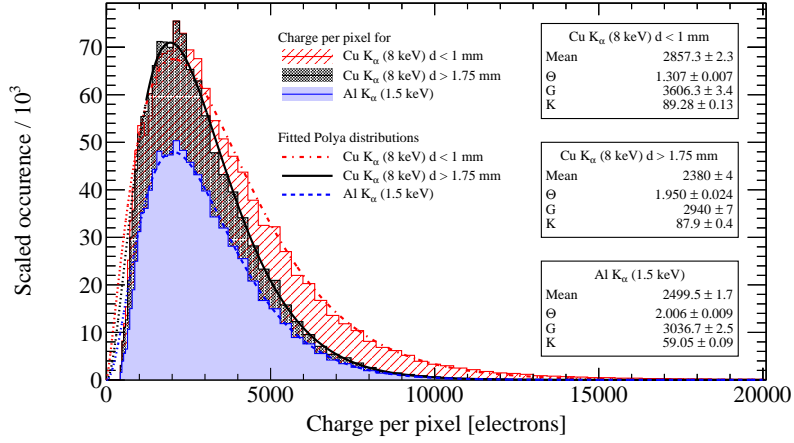


Figure 7: Charge distribution collected by individual pixels in events with 1.5 keV X-ray photons (solid light blue) and 8 keV X-ray photons, the latter split into two distributions: with all pixels in more than 1.75 mm distance to the reconstructed center (black dots) and those closer than 1 mm to the center (red hashes). For each histogram a Polya distribution was fitted to the data, the resulting parameters are given in the boxes on the right.

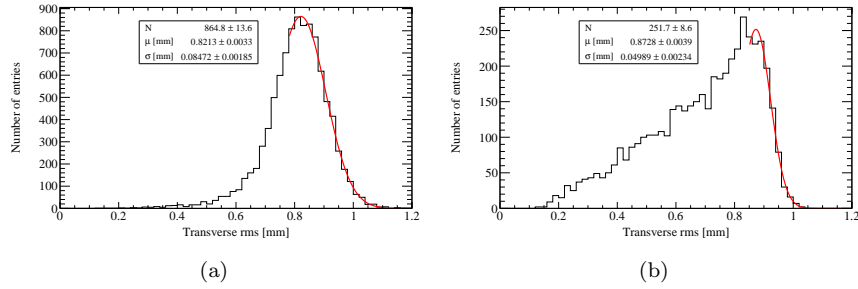


Figure 8: Diffusion of the charge cloud as defined by σ_{trans} . Distribution for 1.5 keV photons (a) and for 8 keV photons (b) are shown. The fit to the right side gives the maximum diffusion.

the maximal cluster size after a 3 cm drift (calculation of $\sigma(3\text{ cm})$ see Sect. 1.3). A Gaussian fit to the right side of the distribution determines the maximum of the distribution and thus gives the diffusion coefficient. The fits result in $D_t \approx 474\text{ }\mu\text{m}/\sqrt{\text{cm}}$ and $D_t \approx 504\text{ }\mu\text{m}/\sqrt{\text{cm}}$ respectively. The slight variations can be attributed to temperature changes between the different measurements.

For the low energetic X-rays a fast drop on the left side indicates, that most of the photons are absorbed close to the cathode, while the slower drop for higher energetic photons shows the higher penetration power of these photons and thus the reduced diffusion for these electron clouds.

The energy dependence of the three eventshape parameters introduced in section 1.3 are shown in Fig. 9. The left column always shows distribution of the 1.5 keV photons and in the right column the energy dependence of the means and the width are shown.

For the fraction $F_{1\sigma_{\text{trans}}}$ of pixels within 1 rms around the center of the charge cloud, the mean approaches about 35% for high energetic photons, which is shown in Fig. 9b. The eccentricity ϵ of higher energetic photons is close to one (see Fig. 9d) indicating a good circularity. The length l divided by σ_{trans} varies between 5 and 6 (see Fig. 9f), which shows that all electrons are contained in the range of $\pm 3\sigma_{\text{trans}}$ as expected from statistical considerations. For tracks parallel to the grid the expected numbers are significantly smaller for $F_{1\sigma_{\text{trans}}}$, larger (up to about 12) for ϵ and also for l/σ_{trans} (up to approximately 35 to 40).

For all three variables, the separation power decreases for lower energetic photons, since the widths of the distributions increases and also the central value shifts. This is due to the smaller number of the primary electrons, where individual electrons experiencing a higher diffusion have more impact.

A simple Monte Carlo simulation was used to study the dependence of the quantities on the statistics. A fixed number of electrons increasing in steps of 10 from 10 to 300 was smeared by a 2D Gaussian distribution with a width corresponding to the maximum diffusion $\sigma(3\text{ cm}) \approx 800\text{ }\mu\text{m}$. The final position of each electron was quantized in steps of $55\text{ }\mu\text{m}$ representing the finite pitch of the GridPix detector. The reconstruction and analysis was done with the same software as for the detector data. The values of the simulations are indicated by thin dashed connecting lines in all graphs. They follow the shape of the curves given by the detector data and small quantitative deviation can be explained by the limited accuracy of the simulation (e.g. neglecting the initial track of the photoelectron in the conversion).

The third and fourth central moments, skewness S and excess kurtosis K , give additional information about the shape of the distribution. Since they are defined in one dimension only, the projection of the hits on the long axis has been chosen. These measures are defined as

$$S_{\text{long}} = \frac{1}{n} \sum_{i=0}^n \frac{(x_i - \mu_x)^3}{\sigma_x^3} \quad (3)$$

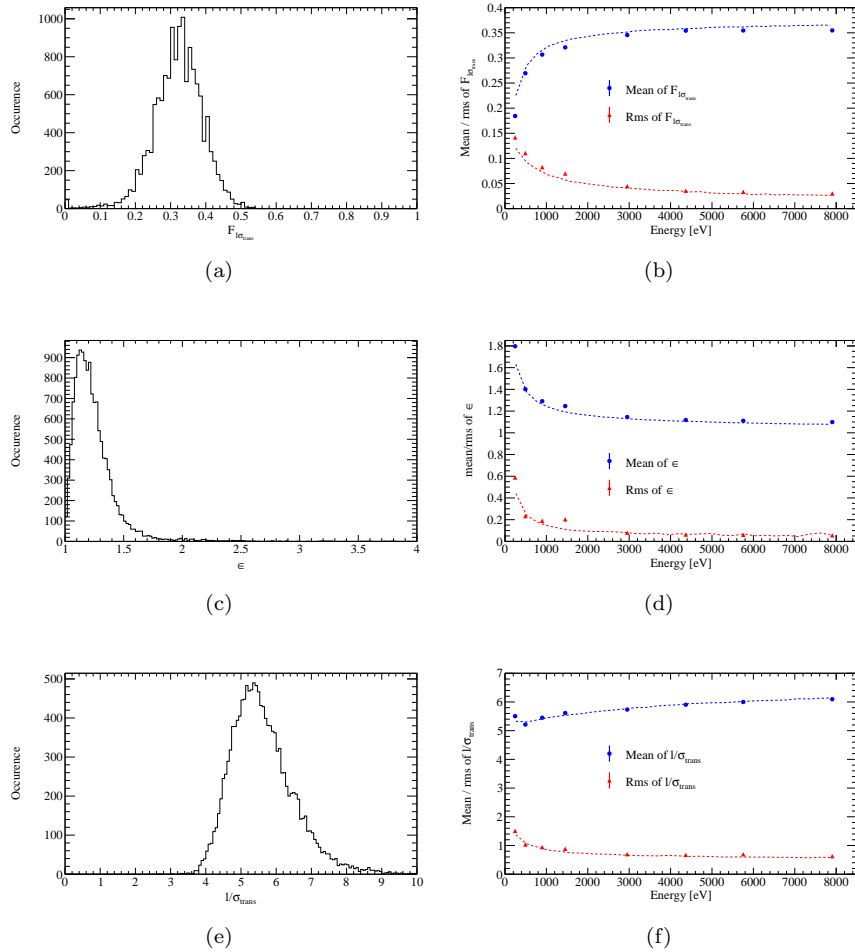


Figure 9: Energy dependence of three eventshape variables. On the left side are example distributions of the 1.5 keV X-rays, on the right side the energy dependencies of the mean and the width are given. The thin dashed lines show the results of a simple Monte Carlo simulation described in the text. The three variables are: fraction $F_{1\sigma_{\text{trans}}}$ of pixels within 1 rms around the reconstructed center, (a) and (b)), eccentricity ϵ , (c) and (d), and length l divided by transverse rms σ_{trans} , (e) and (f).

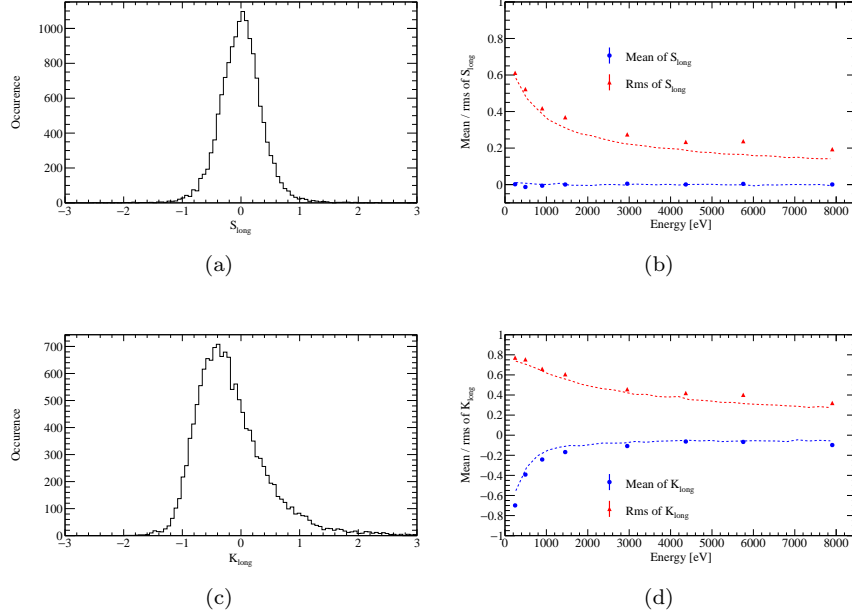


Figure 10: The two central moments skewness S_{long} , (a) and (b), and excess kurtosis K_{long} , (c) and (d). On the left side are example distributions of the 1.5 keV X-rays, on the right side the energy dependencies of the mean and the width are given. The thin dashed lines show the results of a simple Monte Carlo simulation described in the text.

and

$$K_{\text{long}} = \left(\frac{1}{n} \sum_{i=0}^n \frac{(x_i - \mu_x)^4}{\sigma_x^4} \right) - 3 \quad (4)$$

where x_i are the positions of the pixels on the long axis, μ_x is the mean of the x_i and $\sigma_x = \sigma_{\text{long}}$ the rms along the long axis. Fig. 10 shows the two quantities on the left side for the 1.5 keV aluminum K_{α} line, while on the right side the dependence on the energy is shown.

The skewness is centered around 0 indicating that the signals are symmetric around the reconstructed central position. Except a widening of the distribution for lower energetic photons, no variations can be observed. Since tracks are most of the times also symmetric around the reconstructed center, the quantity can not be used for a CAST background suppression.

In Fig. 10 the excess kurtosis is shown as well. Its mean is around zero for higher energetic photons as expected for a normal distribution. However, lower energetic photons show a mean significantly lower, which is a sign of a flatter top than a normal distribution. This is due to a stronger impact of single outlying electrons, determining the long axis and stretching the scale systematically selected for this quantity.

4. Conclusion

An argon/isobutane (97.7%/2.3%)-filled GridPix detector has been successfully tested and calibrated with soft X-rays (277 eV to 8 keV) using the variable energy X-ray source of the CAST Detector Lab at CERN. A good linearity and energy resolution could be demonstrated using both number of hit pixels and total measured charge as energy measures. An energy resolution (σ_E/E) better than 10% (20%) was reached for energies above 2 keV (0.5 keV). Several characteristics of the X-ray events were studied and three eventshape variables were identified which can be used for discrimination of non-X-ray background events in an application at a low rate experiment such as CAST where a low background rate is crucial for increasing the sensitivity for axions and other particles beyond the Standard Model. The energy dependence of these variables has been studied and is well understood.

Acknowledgments

We thank the CAST collaboration for providing access to the CAST Detector Lab facilities, including especially the X-ray generator, and the support in preparing and performing the measurements.

References

- [1] V. Anastassopoulos, et al., New cast limit on the axion-photon interaction, *Nat. Phys.* 13 (2017) 584–590. doi:10.1038/nphys4109.
- [2] V. Anastassopoulos, et al., Search for chameleons with CAST, *Phys. Lett. B* 749 (2015) 172–180. doi:10.1016/j.physletb.2015.07.049.
- [3] C. Krieger, et al., InGrid-based X-ray detector for low background searches, *Nucl. Instr. Meth. Phys. Res. A* 729 (2013) 905 – 909. doi:10.1016/j.nima.2013.08.075.
- [4] T. Vafeiadis, Contribution to the search for solar axions in the CAST experiment, Ph.D. thesis, Aristotle University of Thessaloniki / CERN, CERN-THESIS-2012-349 (November 2012).
- [5] G. E. Villa, et al., The optical/uv filters for the epic experiment, in: 1997 IEEE Nuclear Science Symposium Conference Record, 1997, pp. 618–623. doi:10.1109/NSSMIC.1997.672658.
- [6] A. Thompson, et al., X-ray data booklet, Lawrence Berkeley National Laboratory, University of California, Berkeley, CA 94720, USA, online available at <http://xdb.lbl.gov/> (accessed on Juli 31st, 2017) (October 2009).
- [7] C. Krieger, et al., A GridPix-based X-ray detector for the CAST experiment, *Nucl. Instr. Meth. Phys. Res. A* 867 (2017) 101–107. doi:10.1016/j.nima.2017.04.007.

- [8] X. Llopart, R. Ballabriga, M. Campbell, L. Tlustos, W. Wong, Timepix, a 65k programmable pixel readout chip for arrival time, energy and/or photon counting measurements, *Nucl. Instr. Meth. Phys. Res. A* 581 (2007) 485–494. doi:10.1016/j.nima.2007.08.079.
- [9] M. Chefdeville, P. Colas, Y. Giomataris, H. van der Graaf, E. Heijne, S. van der Putten, C. Salm, J. Schmitz, S. Smits, J. Timmermans, J. Visschers, An electron-multiplying 'micromegas' grid made in silicon wafer post-processing technology, *Nucl. Instr. Meth. Phys. Res. A* 556 (2006) 490–494. doi:10.1016/j.nima.2005.11.065.
- [10] H. van der Graaf, Gridpix: An integrated readout system for gaseous detectors with a pixel chip as anode, *Nucl. Instr. Meth. Phys. Res. A* 580 (2007) 1023–1026. doi:10.1016/j.nima.2007.06.096.
- [11] J. Ottnad, Studies on field distortions and quenching gas properties of an in-grid based x-ray detector, Master's thesis, Physikalisches Institut, Rheinischen Friedrich-Wilhelms-Universitt Bonn (March 2014).
- [12] B. Henke, E. Gullikson, J. Davis, X-Ray Interactions: Photoabsorption, Scattering, Transmission, and Reflection at $E = 50\text{-}30,000$ eV, $Z = 1\text{-}92$, *At. Data Nucl. Data Tables* 54 (2) (1993) 181 – 342. doi:10.1006/adnd.1993.1013.
- [13] J. Abernathy, et al., Marlintpc: A common software framework for tpc development, in: 2008 IEEE Nuclear Science Symposium Conference Record, 2008, pp. 1704–1708. doi:10.1109/NSSMIC.2008.4774731.
- [14] W. Blum, W. Riegler, L. Rolandi, Particle Detection with Drift Chambers, 2nd Edition, Springer-Verlag Berlin Heidelberg, 2008. doi:10.1007/978-3-540-76684-1.